An efficient and multi-focal focused ultrasound technique for harmonic motion imaging

Niloufar Saharkhiz, Graduate Student Member, IEEE,

Hermes A. S. Kamimura, Member, IEEE,

Elisa E. Konofagou, Fellow, IEEE

Department of Biomedical Engineering and Radiology (EEK), Columbia University, New York, NY 10027 USA

Abstract

Harmonic motion imaging (HMI) is an ultrasound-based elasticity imaging technique that utilizes oscillatory acoustic radiation force to estimate the mechanical properties of tissues, as well as monitor high-intensity focused ultrasound (HIFU) treatment. Conventionally, in HMI, a focused ultrasound (FUS) transducer generates oscillatory tissue displacements, and an imaging transducer acquires channel data for displacement estimation, with each transducer being driven with a separate system. The fixed position of the FUS focal spot requires mechanical translation of the transducers, which can be a time-consuming and challenging procedure. In this study, we develop and characterize a new HMI system with a multi-element FUS transducer with the capability of electronic focal steering of ±5 mm and ±2 mm from the geometric focus in the axial and lateral directions, respectively. A pulse sequence was developed to drive both the FUS and imaging transducers using a single ultrasound data acquisition (DAQ) system. The setup was validated on a tissue-mimicking phantom with embedded inclusions. Integrating beam steering with the mechanical translation of the transducers resulted in a consistent high contrast-to-noise ratio (CNR) for the inclusions with Young's moduli of 22 and 44 kPa within a 5-kPa background while the data acquisition speed is increased by 4.5–5.2-fold compared to the case when only mechanical movements were applied. The feasibility of simultaneous generation of multiple foci and tracking the induced displacements is demonstrated in phantoms for applications where imaging or treatment of a larger region is needed. Moreover, preliminary feasibility is shown in a human subject with a breast tumor, where the mean HMI displacement within the tumor was about 4 times lower than that within perilesional tissues. The proposed HMI system facilitates data acquisition in terms of flexibility and speed and can be potentially used in the clinic for breast cancer imaging and treatment.

Keywords

Breast cancer; elastography; electronic beam steering; focused ultrasound (FUS); harmonic motion imaging (HMI); multi-focal FUS

ek2191@columbia.edu .

I. INTRODUCTION

Non-invasive assessment of tissue mechanical properties is greatly valued in medical practice for diagnosis and treatment planning as several diseases such as liver fibrosis [1], [2], breast [3], [4] and prostate cancers [5], thyroid nodules [6] and cardiovascular diseases [7], [8] are associated with alteration of these properties. Ultrasound elasticity imaging techniques have been developed over the past three decades to estimate the mechanical properties of tissues. All these techniques involve excitation of the tissue and monitoring tissue deformation in response to the stimulus to infer tissue properties. The perturbation can be provided using an external excitation as in strain elastography [9] and transient elastography [10], the internal physiologic motion [11]–[13], or acoustic radiation force [14].

Acoustic radiation force-based elasticity imaging techniques utilize a volumetric force resulting from momentum transfer from the ultrasound beam to the propagating medium due to the acoustic absorption. This force generates deformations within the tissue that can be detected using a hydrophone as in vibro-acoustography [15]. The different approaches employ an imaging transducer to estimate the tissue deformation at the location of the applied force (on-axis) as shown in acoustic radiation force impulse imaging [16] and harmonic motion imaging [17], [18] or monitor the tissue response off-axis from excitation as shown in shear wave elasticity (SWE) imaging [19], supersonic shear imaging [20] or comb-push ultrasound shear elastography [21]. An overview of these techniques can be found in [14], [22], [23].

HMI utilizes oscillatory acoustic radiation force to generate harmonic displacements within the tissue [17], [24]. One of the advantages of HMI is the specific frequency of the induced displacements that makes them distinct from various noises such as breathing and motion artifacts. Conventionally, a focused ultrasound (FUS) transducer is used in HMI to transmit an amplitude modulated (AM) signal and induce tissue vibration at the FUS focal spot. The tissue response is tracked using a separate imaging transducer confocally aligned with the FUS transducer through the central opening. The amplitude of the displacements is inversely proportional to the stiffness of the underlying tissue, under some assumptions such as uniformity of stress distribution and tissue homogeneity that are relatively valid for a small FUS focus (~1 mm^3). In a recent study, a less complex HMI setup was proposed in which a single imaging transducer was used to generate and track the harmonic motions [25]. Using a FUS transducer as a source of tissue perturbation not only generates a highly localized mechanical stimulus, especially in the elevation direction, but also provides HMI with the sole objective of diagnosis and elasticity imaging or simultaneously for high-intensity focused ultrasound (HIFU) ablation treatment and monitoring. Several studies have shown the diagnostic application of HMI for characterization of abdominal organs in mice *in vivo* [26], pancreatic cancer in mice *in vivo* and post-surgical human specimens [27], [28] and breast cancer in post-surgical human specimens [29] and human subjects [30]. The therapeutic application of HMI, named harmonic motion imaging-guided focused ultrasound (HMIgFUS), for HIFU ablation and monitoring has been shown in *ex vivo* canine liver [31], *in vivo* pancreatic cancer-bearing mice [31], [32], and post-surgical breast specimens of human subjects as well [33].

A single-element FUS transducer was used in the previous studies to create the oscillatory HMI displacements. The focal spot of the transducer was on the order of a few millimeters and generated a highly localized force that allowed for pinpoint estimation of the mechanical properties. However, in order to image or ablate a clinically relevant volume of tissues, the transducers needed to be translated mechanically in a point-by-point raster scan format [26], [27], [33], [34], which is a relatively slow process. In addition, mechanical movements of the HMI transducers may cause poor acoustic coupling at the interface. To overcome these limitations, a multi-element FUS transducer can be used to move the focal spot electronically in a dramatically shorter time than the transducers' physical movement. The electronic steering of the focal spot is achieved by adjusting phases of the sinusoidally modulated radio frequency (RF) signals that drive each element independently. The electronic beam steering provides a synthetic modification of the focal spot shape, size, and position, as well as simultaneous multiple foci [35]–[39], which increases the overall treatment volume and consequently faster procedures. Several studies have proposed the therapeutic application of phased arrays in hyperthermia [35], [40], [41], thermal surgery [42]–[44], drug delivery [45], [46] and neuromodulation [47]. A recent study showed that electronic steering of the focal spot could be used to image a larger tissue volume in HMI using a 93-element phased array transducer [48]. However, two separate workstations and two ultrasound research systems were used to drive the FUS and imaging transducers separately, limiting the setup's application in the clinical settings in terms of cost and portability. In addition, the steering range was limited to ±1.7 mm laterally and ±2 mm axially.

This study introduces a new HMI setup with electronic beam steering capability using a single ultrasound data acquisition (DAQ) system to drive both the HMI transducers through a customized pulse sequence. A 128-element random phased array is used to increase the steering range in the volumetric space. The feasibility of electronic focal steering in the axial and lateral directions and generation of the simultaneous multiple foci are demonstrated in a tissue-mimicking phantom. Lastly, the preliminary application of the new HMI system for elasticity imaging of an *in vivo* breast tumor is shown in a human subject.

II. Materials and Methods

A. Experimental setup

The HMI oscillatory force was generated using a 128-element FUS transducer (center frequency: 4.5 MHz, diameter: 80 mm, radius of curvature: 76 mm, H265, Sonic Concepts Inc. Bothell, WA, USA). The 4-mm diameter sub-elements were arranged in a randomized configuration instead of a periodic one to reduce the grating lobes [39]. The active area of the transducer was divided into small elements to increase the steering performance. The transducer was connected to an ultrasound research system (256-channel Verasonics Vantage system with the HIFU option, Kirkland, WA, USA) through an RF matching box connected to the first 128 channels of the Vantage system (Fig. 1a). An external HIFU transmit power supply was used to provide continuous high-level output power through each channel. The −6 dB focal region of the FUS transducer at the geometric focus was determined as 0.42 mm (transverse) by 4.19 mm (axial) (Fig. 1b-e) using a lipstick hydrophone (HGL-200,

Onda Corp, Sunnyvale, CA, USA). The resultant displacements were estimated using a 104-element phased-array imaging transducer (center frequency: 7.8 MHz, P12–5, ATL Philips, Bothell, WA, USA) connected to the other 128 channels of the Vantage system. The imaging transducer was confocally aligned through a 41-mm central opening of the FUS transducer.

B. HMI pulse sequence

In order to generate one cycle of AM output signal, 40 transmit waveforms were generated at a fixed transmit voltage but with modulated relative pulse widths. The pulse width modulation (PWM) was programmed by sampling a 50-Hz waveform over 40 points and assigning a different pulse width value to each segment, reflecting the desired output level at that point. The pulse widths were proportional to the transmit voltage level at each segment of the AM output signal (Fig. 2a) and were sinusoidally varied (equal to $\frac{2}{\pi}sin^{-1}\left(\frac{9\cos(x)+11}{20}\right)$ with the period of the signal to be $T = \frac{1}{f_{AM}}$) to form an AM-modulated signal. The HMI pulse sequence was evaluated with the HGL-200 hydrophone in a tank filled with deionized, degassed water. The HMI excitation pulses interleaved with the tracking pulses were generated using a single Verasonics Vantage system (Fig. 2a). In each 500-μs segment, a burst pulse duration of 175μs at the frequency of 4.5 MHz was created. These signals were programmed into the first 128 channels of the Vantage system to drive the FUS transducer. In order to maximize the signal-to-noise ratio (SNR), 10 μs after the burst pulse in each segment, a 1.5 cycle plane-wave pulse at a frequency of 7.8 MHz was programmed to the other 128 channels of the Vantage system to drive the imaging transducer (Fig. 2.c). Therefore, the displacement could be tracked at an imaging pulse repetition frequency (PRF) of 2000 Hz. Four cycles of 50-Hz AM displacements were induced at each spatial location.

C. Electronic beam steering

The beam profiles and intensity changes during electronic beam steering in the axial and lateral directions and the generation of simultaneous multi-foci were verified through hydrophone measurements. The multi-foci were generated by dividing the elements into different groups, and the RF-signal delays corresponding to each focus were applied to each group. The phased array transducer was translated in a water tank using a 3-D positioning system (Velmex Inc., Bloomfield, NY, USA), and the beam profile at a low power was measured using the lipstick hydrophone. A fiber-optic hydrophone (HFO-690, Onda Corp, Sunnyvale, CA, USA) was used to measure the pressure profile of steered beams at high powers. The signals were sampled using a 200 MHz high-speed and high-resolution PicoScope (Model 5242D, Pico Technology, UK) through MATLAB (R2017b).

D. HMI data acquisition – phantom experiments

A custom elasticity phantom with embedded cylindrical inclusion (Background Young's modulus: 5.3 kPa, inclusions Young's moduli: 22 and 44 kPa, inclusion diameter: 6.5 and 10.4 mm, speed of sound: 1530–1550 m/s, attenuation: 0.50 ± 0.05 dB/cm at 1 MHz; custom model, CIRS, Norfolk, VA, USA) was used. The phantom was immersed in a water tank filled with deionized, degassed water with a layer of sound-absorbing material placed at the

bottom of the tank to reduce the undesired echoes. The HMI transducers were placed in the tank using the 3-D positioning system. First, the focal spot was set at the geometric focus within the phantom background, where 4 cycles of 50-Hz AM displacements were induced and tracked. Then the axial and lateral steering ranges were tested by electronically moving the focal spot −5, −2, −1, +1, +2, and +5 mm axially and from −2 to 2 mm by 1-mm step size laterally from the geometric focus with 4 cycles of induced HMI displacements at each location. To note, a few milliseconds were allowed between switching the location of the focal spot to allow recovery of the medium and avoid shear wave propagation interference between different locations. Second, the feasibility of the generation of simultaneous multi-foci was tested in the phantom background. The elements of the FUS transducer were divided into two groups, and each group was programmed with independent delays corresponding to a separate focal spot, where the 2 foci separated by 2 mm laterally were generated. The experiment was repeated with a 4 mm lateral distance between the two foci.

Lastly, in order to image the inclusions embedded within the background of the phantoms, two approaches were taken: 1) mechanical translation of the HMI transducers using the 3-D positioner in a point-by-point raster scan pattern, using the parameters given in Table I and generating the HMI force only at the geometric focus (no electronic steering) at each point (Fig. 3). The transducers remained for 3 seconds at each point, where160 frames were acquired at the PRF of 2000 Hz after transducer stabilization with 500 ms spent for data acquisition and storing. Thus, the total time for data acquisition throughout the mechanical translation of the transducers spanned within 220.5 seconds to image the 6.5-mm diameter inclusion and 1102.5 seconds to image the 10.4-mm diameter inclusion. 2) combined mechanical translation of the transducers and electronic steering of the focal spot from −4 to 4 mm axially in 2 mm steps and from −2 to 2 mm laterally in 1-mm steps (25 locations including the geometric focus) at each raster imaging location (Fig. 3). The raster scan parameters for the combined approach are given in Table I.

The sequence was programmed so that the focal spot was steered consecutively after inducing 4 cycles of HMI displacement at each location. Therefore, the time needed to steer the focal spot, acquire and store the data from the 25 electronic steering points was about 4 seconds, resulting in a total imaging time of 42 and 210 seconds to image the inclusions with the diameters of 6.5 and 10.4 mm, respectively. (42) seconds, including the 3-second pause between two consecutive mechanical scan points. The mechanical translation of the transducers was necessary for the second approach since the region of interest (ROI), including the inclusions and their background medium, were larger than the electronic steering ranges.

E. HMI data acquisition – in vivo human breast

A 23-year-old female patient with a 2.8-cm breast mass diagnosed as fibroadenoma was recruited in accordance with institutional review board (IRB) guidelines and regulations, under a protocol approved by the IRB of Columbia University (Protocol AAAQ9526). A sonographer located the tumor using an ultrasound scanner (Butterfly iQ, Butterfly Network, Inc, Guilford, CT) with the patient lying supine and placed the HMI transducer assembly on top of the breast with a thin ultrasound gel pad in between to provide the acoustic coupling.

The HMI transducer assembly was attached to a 1-D slider (Velmex Inc., Bloomfield, NY, USA) controlled by a PC workstation to acquire data in a point-by-point mechanical raster scan format in the lateral direction. This was necessary since the width of the ROI of 40 mm was larger than the maximum electronic steering range in the lateral direction (±2 mm). The step size of the mechanical scan was set to 5 mm to provide overlap between every two consecutive points, resulting in moving the transducers mechanically to 9 lateral points. At each mechanical raster scan point, the focal spot was electronically steered from –4 to 4 mm in 2-mm increments axially and from –2 mm to 2 mm in 1 mm increments laterally from the geometric focus. At every electronic steering point, 2 cycles of displacement at an AM frequency of 50 Hz were induced during which 80 frames of channel data at a PRF of 2000 Hz were acquired and stored for offline processing. The total imaging time was about 32 seconds during which the data acquisition and storage took about 500 ms, and the transducers were paused for about 3 seconds to become stabilized.

F. HMI displacement estimation

The HMI displacements were processed offline in MATLAB (MATLAB 2019a, MathWorks, Natick, MA, USA). A delay-and-sum beamforming algorithm was applied to reconstruct the beamformed RF data. Three second-order Butterworth notch filters at the fundamental, second and third harmonic of the FUS (4.5, 9, and 13.5 MHz) were applied to suppress the FUS interference. A 1-D normalized cross-correlation algorithm [49] with a window size of 0.85 mm and 95% overlap was applied to the filtered data to estimate the interframe axial displacements. Next, a 2nd order band-pass Chebyshev filter was applied to the axial displacements along the temporal space to extract the 50-Hz HMI displacements. Finally, the mean peak-to-peak oscillations over all the cycles were calculated at each pixel to reconstruct a 2-D HMI displacement map. The aforementioned steps were repeated for each electronic focal spot steering point and mechanical raster scan. For each point, a rectangular ROI with the dimensions of 0.5 mm (lateral) by 1 mm (axial) was selected around the focal spot within the 2-D HMI displacement map. In the case of electronic steering, the ROI was moved from the geometric focus to match the corresponding steering distance. Using the data at each point, the final 2-D HMI displacement map of the inclusion and background medium could be reconstructed.

The reported HMI displacement values in this study are mean ± standard deviation averaged within a rectangular ROI selected manually within the inclusions and the background at the same depth. The width and height of the ROI within the inclusions were set to be 40% of the inclusion's diameter. Two ROIs were considered in the background on both sides of the inclusions, with the height and width equal and half of the inclusions' ROI, respectively. Two metrics of contrast to noise (CNR) and contrast were defined as

$$CNR = \left| \mu_b - \mu_i \right| / \sqrt{\sigma_b^2 + \sigma_i^2} \tag{1}$$

and

$$Contrast = \left| \mu_b - \mu_i \right| / \mu_b, \tag{2}$$

where μ_b, μ_i, σ_b and σ_i are the mean HMI displacement of the background, mean HMI displacement of the inclusion, standard deviation of the HMI displacements within the background, and standard deviation of the HMI displacements within the inclusion. These values were calculated within the ROIs defined above.

III.   Results

A.   Axial focus steering

The focal spot of the FUS transducer was electronically steered in the axial direction, and the pressure profile was measured in the free field using the lipstick hydrophone to estimate the pressure loss and beam-shape changes due to beam steering. Fig. 5a shows the pressure field with the axial steering at −5, −2, −1, 0, 1, 2, and 5 mm relative to the geometric focal spot. The pressure fields are normalized with respect to the maximum pressure measured at the geometric focus. The respective HMI displacement maps acquired in the homogenous background part of the phantom are shown in Fig. 5b. These maps are generated as a result of normalized cross-correlation between the frames acquired 10 ms after the FUS pulse trigger and the baseline frames. The displacement maps are normalized by the maximum displacement value of the map corresponding to the geometric focus at the same time-point.

Hydrophone measurements revealed an intensity drop-off of less than −3 dB for ±2 mm, about −6 dB for +5 mm, and greater than −6 dB for −5 mm axial steering (Fig. 6a) as a result of focusing along the axial direction around the geometric focus. Thus, the focus was steered axially for up to 4 mm in both axial directions for the phantom studies. The maximum peak-to-peak displacement for each map (Fig. 5b) normalized by the maximum displacement at the geometric focus is shown in Fig. 6a in blue color. A comparison between the actual location of the focal spot using the highest value on the pressure map measured by the hydrophone and the intended axial steering distance showed a great correlation (r^2 = 0.9796) (Fig. 6b). The percentage errors between the intended and actual axial steering distance were found to be equal to 13.4, 2.98, 10.45, 40.30, 25.38, and 23.53% for steering distances of −5, −2, −1, 1, 2, and 5 mm from the geometric focus, respectively. Similarly, a linear regression between the location with maximum peak-to-peak displacement amplitude and the intended steering distance revealed an excellent r^2 value of 0.9982 (Fig. 6c). The −6 dB axial focal length measured with the hydrophone was found to have an overall increase trend (r^2 = 0.6424) as the focus was steered away from the transducer (Fig. 6c). The focal spot became slightly more elongated in the axial direction as the focus was steered away from the transducer and shortened as the focus was steered towards the transducer (Fig. 5b and Fig. 6c). Fig. 6d shows the relative grating lobe intensity levels with respect to the maximum intensity of the main lobe. Accordingly, the grating lobe level decreased by moving the focus away from the transducer and increased closer to it with the greatest grating lobe level of −3.1 dB at −5 mm steering distance from the geometric focus.

B.   Lateral focus steering

The hydrophone-measured beam maps depicting the lateral beam steering are shown in Fig. 7a. The beam was steered from −2 to 2 mm in 1-mm steps. The HMI displacement maps acquired 10 ms after the FUS beam trigger in the phantom background show a downward

trend in the displacement as a result of pressure loss due to the steering (Fig. 7b). The intensity decrease due to lateral steering was quantified using the lipstick hydrophone and are demonstrated in Fig. 8a (circles). The most significant intensity drops were measured as −5 and −19.6 dB by steering the focus for −2 and +2 mm laterally from the geometric focus. The corresponding maximum peak-to-peak displacement normalized by the maximum displacement at the geometric focus decreased by moving the focus laterally around the geometric focus as expected (blue). Fig. 8b depicts the intended lateral steering distances and the actual steering distances calculated based on the maximum pressure maps (circle) and maximum displacements (triangle) values. The linear regression fit obtained from the actual and intended lateral steering distances resulted in an excellent agreement (r^2 values of 0.9800 and 0.9959 for the actual distance based on the pressure and displacement data, respectively). The percentage errors between the intended and actual lateral steering distance based on the pressure values were found to be equal to −36, 57.33, 13.78, and 8.44% for steering distances of −2, −1, 1, and 2 mm from the geometric focus, respectively. Fig. 8c shows the −6 dB focal length in millimeters as the beam was steered around the geometric focus in the lateral direction. The focal length was found to only slightly decrease, with the focal length to be 0.91 and 0.92 at the lateral distances of −2 and 2 mm, respectively, to the one at the geometric focus. Lastly, the grating lobe level normalized by the maximum intensity at the main lobe is shown in Fig. 8d, where a maximum grating level of −10.12 dB was calculated for moving the focus in the lateral direction for −2 mm, and 4.04 dB was calculated for +2-mm lateral steering.

C. Multi-focal HMI

In Fig. 9, the pressure profiles measured with the hydrophone in the free field, corresponding 2-D HMI displacement maps and −6 dB displacement regions are illustrated for a single focus (a-c), two foci separated by 2 mm (d-f) and two foci separated by 4 mm (g-i) in the lateral direction. The maximum displacements with respect to the maximum displacement at the geometric focus were 0.41 and 0.22 within the HMI maps resulting from multi-foci separated by 2 and 4 mm, respectively. However, the corresponding −6 dB displacement regions were 2.17 and 2.56 times the one generated by the single focus.

D. HMI on tissue-mimicking phantoms

Figure 10 demonstrates the B-mode images (a-d), 2-D peak-to-peak HMI displacement maps (e-h and m-p), and 2-D normalized HMI displacement maps (i-l and q-t) of 22 and 44 kPa inclusions embedded within the 5 kPa background. The images are generated through two data acquisition scenarios described previously (mechanical raster scanning and combined mechanical raster scanning and electronic beam steering, as shown in Fig. 3). The mean peak-to-peak HMI displacement was found to be 0.92±0.04 (1.02±0.07) μm and 0.72±0.05 (0.75±0.04) μm for the 6.5 and 10.4-mm diameter inclusions with Young's modulus of 22 kPa and 0.74±0.02 (0.78±0.03) μm and 0.51±0.02 (0.54±0.01) μm for the 6.5 and 10.4-mm diameter inclusions with Young's modulus of 44 kPa where the data was acquired through mechanical translation (mechanical translation combined with electronic steering) of the transducers. The 2-D normalized displacement maps were used to calculate the CNR and contrast for each image. Accordingly, the CNR was estimated to be 10.41 (6.21) and 13.39 (11.63) for the 6.5 and 10.4-mm diameter inclusions with

Young's modulus of 22 kPa and 12.94 (10.17) and 9.79 (9.55) for the 6.5 and 10.4-mm diameter inclusions with Young's modulus of 44 kPa where the data was acquired through mechanical translation (mechanical translation combined with electronic steering) of the transducers. The contrast values were estimated to be 0.25 (0.24) and 0.45 (0.45) for the 6.5 and 10.4-mm diameter inclusions with Young's modulus of 22 kPa and 0.37 (0.39) and 0.58 (0.57) for the 6.5 and 10.4-mm diameter inclusions with Young's modulus of 44 kPa, where the data was acquired through mechanical translation (mechanical translation combined with electronic steering) of the transducers.

E. HMI in an in vivo human breast tumor

Figure 11 is an example representing the application of the new HMI setup with electronic focal steering capability for human breast tumor characterization in a patient (23 years old, diagnosed with a 2.8 cm-Fibroadenoma). The B-mode images of the benign tumor acquired with the Butterfly iQ and the 7.8-MHz imaging transducer are shown in Fig. 11a and b, respectively. The tumor is delineated using white-dashed lines. The 2-D HMI displacement map is illustrated in Fig. 11c, which is reconstructed based on the induced HMI displacements at each location of the mechanical raster scan and electronic focal steering. The map is normalized by using the average of a few lines in the lateral direction to compensate for the acoustic attenuation along the axial depth and acoustic pressure changes due to the electronic beam steering. Accordingly, the mean HMI displacement within the tumor was estimated to be 1.17 ± 0.04 μm, whereas the HMI displacement within the depth match surrounding tissue was found to be 4.78 ± 0.37 μm.

IV. Discussion

This study sought to develop and characterize a new HMI setup with electronic focal steering capability using a single ultrasound data acquisition (DAQ) system. A customized pulse sequence was developed, which was composed of an AM signal generated through PWM technique programmed to the half of the channels to drive the FUS transducer and generate harmonic displacements, interleaved with the tracking pulses programmed to the other half of the channels to drive the imaging transducer and track the induced harmonic displacements. The conventional HMI system is composed of a single element FUS transducer driven by a function generator and RF amplifier, as well as an imaging transducer driven by an ultrasound DAQ system. The proposed setup in this study eliminates the need for a function generator and an RF amplifier, making the HMI system compact and cost-efficient.

In addition to the complexity and size of the conventional HMI setup, the acoustic radiation force for a single-element FUS can only be generated at a fixed depth (i.e., geometric focus) which is on the order of a few millimeters. Therefore, mechanical translation of the HMI transducers was necessary to image a large region such as a tumor. Although the precise imaging capability of HMI is an advantage of the method compared to the other elasticity imaging techniques, the mechanical movements are slow and time-consuming [30]. Additionally, variation of the tissue pre-compression, loss of acoustic coupling between the tissue and transducer, and dragging of the tissue, especially during imaging of a

curved surface such as the breast, are among the drawbacks associated with the mechanical movement of the transducers. A recent study showed the possibility of focal electronic steering to minimize the mechanical movements of the transducers. However, two DAQ systems were needed to drive the HMI transducers separately [48]. Combining electronic beam steering with mechanical raster scanning not only resolves some of the limitations associated with the mechanical translation of the transducers but also significantly shortens the entire procedure. In fact, electronic focal steering in both axial and lateral directions reduced the number of mechanical raster scan points by 5 times in each direction and speeded up the imaging time by 3.5 times to image a small (6.5-mm diameters) inclusion and 4.5 times to image a larger (10.4-mm diameter) inclusion, compared to a scenario where only mechanical translation of the transducers was used. Moreover, in some cases where mechanical movement of the HMI assembly in the axial direction is not possible due to either loss of acoustic coupling between the skin/transducer interface or compression of the tissues, electronic axial focal steering could be helpful to directly assess the mechanical properties of the tissue around the geometric focus.

Every cycle of the 50-Hz AM signal was divided into 40 segments, each containing 175 μs (35% duty cycle in each segment) of a continuous pulse at 4.5 MHz, followed by a tracking pulse at 7.8 MHz with a delay of 10 μs, resulting in an interleaving sequence of FUS and imaging pulses (Fig. 2). This sequence was programmed in order to image the displacements in the absence of FUS beams to increase the SNR. However, the imaging and FUS transducers can also be simultaneously driven if required, as shown by Lee et al. [50]. A duty cycle of 35% was used for the FUS pulses in each segment of the AM signal and was powerful enough to induce micron-size displacements within the underlying medium. It is expected that the response of the underlying medium is different compared to the case where the ARF is applied continuously and should be further investigated. Here, the duty cycle was selected to have less exposure to ARF, as well as due to the limitations of the external HIFU transmit power supply and the relatively low efficiency of the FUS transducer (40% for each individual channel into the matching network, and 70% efficiency into the element, according to the manufacturer). A recent study using ST-HMI has shown that the duty cycle of the excitation pulse does not have a significant impact on the contrast and CNR of the inclusions [25]. Therefore, the duty cycle can be reduced to minimize the induced heat deposition without compromising the technique's performance for imaging purposes [25]. A secondary external power supply can be added to achieve 100% a duty cycle of the FUS pulses when a continuous exposure is needed for applications such as HMIgFUS to get a rapid and intense tissue heating if needed [33].

The intensity of the main beam was found to be reduced by moving the focus away from the geometric focus in both axial and lateral directions (Fig. 5–8). The amplitude of the displacements during axial focal steering was a function of both the pressure loss due to steering and acoustic attenuation of the phantom (0.5 dB/MHz/cm). The attenuation is the reason for lower decrease in the displacement values at lower depths compared to the drastic decrease in the hydrophone measurements at those depths (Fig. 5b and Fig. 6a). The steering range was set to be ±4 mm in the axial and ±2 mm in the lateral directions to limit the intensity drop-off to less than −3 dB. The asymmetry in intensity drop-off as a result of lateral steering, especially for steering distances of ±2 mm (Fig. 8a), can be attributed

to the transducer configuration including number of elements, element size, aperture size, randomized positioning of the elements, wavelength and experimental limitations that led to a slight misalignment during steering characterization, resulting in out-of-plane steering. A larger steering range can be achieved using a transducer with more elements or reducing the size of the elements. The latter results in lower power from each element; thus, a higher input voltage might be needed to compensate [37]. Although the estimated displacement values were subject to jitter and underestimation [51] and about 1 dB error was limited by the hydrophone readings (according to the manufacturer), an excellent correlation was found between the actual and intended steering distances (Fig. 6b and Fig. 8b).

Multi-element focused therapeutic transducers generally have large apertures to provide high enough intensity for tissue heating and ablation. Ideally, the inter-element spacing should be minimized to reduce the generation of grating lobes since the spacing larger than $\lambda/2$, where λ is the ultrasound wavelength, results in undesired grating lobes [37], [52]. The inter-element spacing can be reduced by increasing the number of elements, yet this leads to more complexity and higher costs. One way to reduce the intensity of the grating lobes is to design the array with randomized sparse elements to distribute the energy incoherently away from the main focus [37], which was implemented in the customized transducer in this study. The intensity of the grating lobes increased with respect to the main beam by moving the focus towards the transducer and decreased by moving the focus away from the transducer in the axial direction (Fig. 5–6). Their relative intensity also increased by moving the focus away from the geometric focus in the lateral direction (Fig. 7–8). The presence of grating lobes did not limit the displacement imaging in this study but should be controlled and minimized during HIFU ablation treatment to avoid undesired tissue heating at sites other than the main lobe. Broad banding [53], deactivation of the subset of the elements [54], optimization of amplitude and phase distribution of each element using a genetic algorithm [55], and apodization are among the techniques for further reduction of the grating lobes that can be implemented in the future studies.

The feasibility of generating two foci simultaneously was shown in this study where the −6 dB excited region was found to be 2.17 (2.56) times larger where the foci were separated by 2 (4) mm in the lateral direction in comparison to the region created by a single focus (Fig. 9). This can be extended to any configuration of multiple foci to engage a larger volume of the tissue and maximize energy deposition in a certain time during applications such as HIFU ablation in HMIgFUS [33] to speed up the procedure since heating a clinically-relevant volume of tissue such as tumor using a single focus can be an impractically lengthy procedure. To note, a pressure drop of −6.65 (−9.26) dB was observed to form two foci separated by 2 (4) mm with respect to the maximum pressure at the geometric focus (Fig. 9a). This can be compensated by increasing the input voltage to the FUS transducer if needed.

The electronic focal steering at 25 points (−4 to 4 mm in 2 mm steps in the axial direction and −2 to 2 in 1 mm steps in the lateral direction from the geometric focus) was combined with the mechanical translation of the transducers to image the inclusions embedded within the tissue-mimicking phantom. Larger regions of interest than the steering distances necessitated the mechanical movements. The HMI displacements decreased at

lower depths in the background part of the phantom due to the radiation force attenuation along the axial direction (Fig. 10e-h and Fig. 10m-p). Thus, the 2-D HMI displacement maps were normalized with respect to the average of a few lateral lines to account for the attenuation. For both imaging scenarios shown in Fig. 3, the inclusions appeared larger on the 2-D HMI displacement maps than the B-mode images (Fig. 10), which are consistent with other elasticity imaging studies and are postulated to be due to the connectivity within the medium. The CNR and contrast values were generally higher for stiffer and larger inclusions. Moreover, similar peak-to-peak HMI displacements were estimated for both data acquisition scenarios. For the smaller inclusions (i.e., 6.5 mm diameter), the CNR values for the data acquired through combined mechanical translation and beam steering were lower compared to the ones for the data acquired through mechanical raster scanning (40.35% and 21.41% decrease in CNR for the inclusions with Young's moduli of 22 and 44 kPa, respectively. A previous study has shown that for accurate measurement of the mechanical properties of an inclusion with HMI, the diameter of the inclusion must be at least 2 times larger than the focal length of the FUS transducer [56]. The sensitivity of the new setup to detect small inclusions will be investigated as a part of a future study. However, for larger inclusions (i.e., diameter of 10.4 mm), the CNR values for the data acquired through the combined data acquisition scenario were only slightly lower than those acquired through mechanical scanning (13.14% and 2.45% decrease in CNR values for the inclusions with Young's moduli of 22 and 44 kPa, respectively). Nevertheless, the time for data collection using combined mechanical raster scanning and electronic beam steering was 4.5–5.2 times lower than that for point-by-point mechanical raster scanning of the transducers. Accordingly, the combined data acquisition technique can significantly reduce the imaging time, which is a major advantage, especially in clinical settings.

The feasibility of imaging an *in vivo* breast tumor in a human subject was demonstrated using the new HMI setup through combined electronic focal steering and mechanical raster scanning in the presence of breathing artifacts. Again, the mechanical translations were unavoidable as the width of ROI was larger than the lateral steering range. The displacements within the benign tumor (2.8-cm Fibroadenoma) were lower than those within the surrounding tissues. The variation of the HMI displacements within the surrounding tissues is due to the inherent inhomogeneous composition of breast tissue. The total scan time was about 32 seconds, during which the transducers were moved to 9 lateral directions mechanically, and an ROI with a width of 40 mm was imaged. The imaging time could have been increased by about 3.5 folds during data acquisition with the sole mechanical translation of the focal spot.

V.   Conclusion

In this paper, a new HMI setup with electronic focal steering capability using a multi-element FUS transducer was developed and characterized. Both the HMI imaging and FUS transducers were driven using a single ultrasound data acquisition system through a customized pulse sequence. The feasibility of imaging inclusions with different geometries and/or stiffnesses embedded within a tissue-mimicking phantom was shown. In addition, the clinical potential of the setup was demonstrated by imaging an *in vivo* human breast tumor where the tumor could be differentiated from the non-cancerous surrounding tissues. Lastly,

simultaneous generation of multiple foci was achieved that enlarges the engaged region. The size and flexibility of the HMI system have improved, and the data acquisition has accelerated compared to the previous settings, which are critical in clinical settings.

Acknowledgment

REFERENCES

[1]. Ferraioli G. et al. , "WFUMB guidelines and recommendations for clinical use of ultrasound elastography: Part 3: Liver," Ultrasound Med. Biol, vol. 41, no. 5, pp. 1161–1179, May 2015, doi: 10.1016/j.ultrasmedbio.2015.03.007. [PubMed: 25800942]

[2]. Friedrich-Rust M. et al. , "Performance of Acoustic Radiation Force Impulse imaging for the staging of liver fibrosis: A pooled meta-analysis," J. Viral Hepat, vol. 19, no. 2, pp. e212–e219, Feb. 2012, doi: 10.1111/j.1365-2893.2011.01537.x. [PubMed: 22239521]

[3]. Garra BS et al. , "Elastography of breast lesions: Initial clinical results," Radiology, vol. 202, no. 1, pp. 79–86, Jan. 1997, doi: 10.1148/radiology.202.1.8988195. [PubMed: 8988195]

[4]. Samani A, Zubovits J, and Plewes D, "Elastic moduli of normal and pathological human breast tissues: an inversion-technique-based investigation of 169 samples," Phys. Med. Biol, vol. 52, no. 6, pp. 1565–1576, Mar. 2007, doi: 10.1088/0031-9155/52/6/002. [PubMed: 17327649]

[5]. Salomon G. et al. , "Evaluation of Prostate Cancer Detection with Ultrasound Real-Time Elastography: A Comparison with Step Section Pathological Analysis after Radical Prostatectomy," Eur. Urol, vol. 54, no. 6, pp. 1354–1362, Dec. 2008, doi: 10.1016/j.eururo.2008.02.035. [PubMed: 18374470]

[6]. Cantisani V. et al. , "Ultrasound elastography in the evaluation of thyroid pathology. Current status," Eur. J. Radiol, vol. 83, no. 3, pp. 420–428, Mar. 2014, doi: 10.1016/j.ejrad.2013.05.008. [PubMed: 23763859]

[7]. De Korte CL, Cespedes EI, Van Der Steen AFW, Pasterkamp G, and Bom N, "Intravascular ultrasound elastography: Assessment and imaging of elastic properties of diseased arteries and vulnerable plaque," Eur. J. Ultrasound, vol. 7, no. 3, pp. 219–224, Aug. 1998, doi: 10.1016/S0929-8266(98)00043-3. [PubMed: 9700219]

[8]. Geier B. et al. , "Ultrasound elastography for the age determination of venous thrombi. Evaluation in an animal model of venous thrombosis," Thromb. Haemost, vol. 93, no. 2, pp. 368–374, Feb. 2005, doi: 10.1160/TH04-07-0437. [PubMed: 15711756]

[9]. Ophir J, Céspedes I, Ponnekanti H, Yazdi Y, and li X, "Elastography: A quantitative method for imaging the elasticity of biological tissues," Ultrason. Imaging, vol. 13, no. 2, pp. 111–134, Apr. 1991, doi: 10.1177/016173469101300201. [PubMed: 1858217]

[10]. Sandrin L. et al. , "Transient elastography: A new noninvasive method for assessment of hepatic fibrosis," Ultrasound Med. Biol, vol. 29, no. 12, pp. 1705–1713, Dec. 2003, doi: 10.1016/j.ultrasmedbio.2003.07.001. [PubMed: 14698338]

[11]. Dickinson RJ and Hill CR, "Measurement of soft tissue motion using correlation between A-scans," Ultrasound Med. Biol, vol. 8, no. 3, pp. 263–271, 1982, doi: 10.1016/0301-5629(82)90032-1. [PubMed: 7101574]

[12]. Wilson L, "Ultrasonic measurement of small displacements and deformations of tissue," Ultrason. Imaging, vol. 4, no. 1, pp. 71–82, Jan. 1982, doi: 10.1016/0161-7346(82)90006-2. [PubMed: 7199773]

[13]. De Korte CL and Van Der Steen AFW, "Intravascular ultrasound elastography: An overview," in Ultrasonics, May 2002, vol. 40, no. 1–8, pp. 859–865, doi: 10.1016/S0041-624X(02)00227-5. [PubMed: 12160059]

[14]. Doherty JR, Trahey GE, Nightingale KR, and Palmeri ML, "Acoustic radiation force elasticity imaging in diagnostic ultrasound," IEEE Trans. Ultrason. Ferroelectr. Freq. Control, vol. 60, no. 4, pp. 685–701, 2013, doi: 10.1109/TUFFC.2013.2617. [PubMed: 23549529]

[15]. Fatemi M. and Greenleaf JF, "Vibro-acoustography: An imaging modality based on ultrasound-stimulated acoustic emission," 1999. Accessed: Mar. 31, 2020. [Online]. Available: www.pnas.org.

[16]. Nightingale KR, Palmeri ML, Nightingale RW, and Trahey GE, "On the feasibility of remote palpation using acoustic radiation force," J. Acoust. Soc. Am, vol. 110, no. 1, pp. 625–634, Jul. 2001, doi: 10.1121/1.1378344. [PubMed: 11508987]

[17]. Konofagou EE and Hynynen K, "Localized harmonic motion imaging: theory, simulations and experiments.," Ultrasound Med. Biol, vol. 29, no. 10, pp. 1405–13, Oct. 2003, Accessed: Oct. 07, 2018. [Online]. Available: http://www.ncbi.nlm.nih.gov/pubmed/14597337. [PubMed: 14597337]

[18]. Maleke C, Luo J, Gamarnik V, Lu XL, and Konofagou EE, "Simulation study of Amplitude-Modulated (AM) Harmonic Motion Imaging (HMI) for stiffness contrast quantification with experimental validation," Ultrason. Imaging, vol. 32, no. 3, pp. 154–176, 2010, doi: 10.1177/016173461003200304. [PubMed: 20718245]

[19]. Sarvazyan APOVSDJBSY, "Shear wave elasticity imaging: a new ultrasonic technology of medical diagnostics.," Ultrasound Med. Biol, vol. 24, no. 9, pp. 1419–35, Nov. 1998, Accessed: Oct. 07, 2018. [Online]. Available: http://www.ncbi.nlm.nih.gov/pubmed/10385964. [PubMed: 10385964]

[20]. Bercoff J, Tanter M, and Fink M, "Supersonic shear imaging: a new technique for soft tissue elasticity mapping," IEEE Trans. Ultrason. Ferroelectr. Freq. Control, vol. 51, no. 4, pp. 396–409, Apr. 2004, doi: 10.1109/TUFFC.2004.1295425. [PubMed: 15139541]

[21]. Song P, Zhao H, Manduca A, Urban MW, Greenleaf JF, and Chen S, "Comb-push ultrasound shear elastography (CUSE): A novel method for two-dimensional shear elasticity imaging of soft tissues," IEEE Trans. Med. Imaging, vol. 31, no. 9, pp. 1821–1832, 2012, doi: 10.1109/TMI.2012.2205586. [PubMed: 22736690]

[22]. Li GY and Cao Y, "Mechanics of ultrasound elastography," Proceedings of the Royal Society A: Mathematical, Physical and Engineering Sciences, vol. 473, no. 2199. Royal Society, Mar. 01, 2017, doi: 10.1098/rspa.2016.0841.

[23]. Sigrist RMS, Liau J, El Kaffas A, Chammas MC, and Willmann JK, "Ultrasound elastography: Review of techniques and clinical applications," Theranostics, vol. 7, no. 5. Ivyspring International Publisher, pp. 1303–1329, 2017, doi: 10.7150/thno.18650. [PubMed: 28435467]

[24]. Maleke C. and Konofagou EE, "Harmonic motion imaging for focused ultrasound (HMIFU): a fully integrated technique for sonication and monitoring of thermal ablation in tissues," Phys. Med. Biol, vol. 53, no. 6, pp. 1773–1793, Mar. 2008, doi: 10.1088/0031-9155/53/6/018. [PubMed: 18367802]

[25]. MM H, N S, and EE K, "Feasibility of Harmonic Motion Imaging Using a Single Transducer: In Vivo Imaging of Breast Cancer in a Mouse Model and Human Subjects," IEEE Trans. Med. Imaging, vol. 40, no. 5, pp. 1390–1404, May 2021, doi: 10.1109/TMI.2021.3055779. [PubMed: 33523806]

[26]. Payen T. et al. , "Elasticity mapping of murine abdominal organs *in vivo* using harmonic motion imaging (HMI)," Phys. Med. Biol, vol. 61, no. 15, pp. 5741–5754, 2016, doi: 10.1088/0031-9155/61/15/5741. [PubMed: 27401609]

[27]. Payen T. et al. , "Harmonic motion imaging of pancreatic tumor stiffness indicates disease state and treatment response," Clin. Cancer Res, vol. 26, no. 6, pp. 1297–1308, Mar. 2020, doi: 10.1158/1078-0432.CCR-18-3669. [PubMed: 31831559]

[28]. Nabavizadeh A. et al. , "Noninvasive Young's modulus visualization of fibrosis progression and delineation of pancreatic ductal adenocarcinoma (PDAC) tumors using Harmonic Motion Elastography (HME) in vivo," Theranostics, vol. 10, no. 10, pp. 4614–4626, 2020, doi: 10.7150/thno.37965. [PubMed: 32292518]

[29]. Han Y, Wang S, Payen T, and Konofagou E, "Human Breast Tumor Characterization on Post-Surgical Mastectomy Specimens Using Harmonic Motion Imaging (HMI)," in IEEE International Ultrasonics Symposium, IUS, Oct. 2017, doi: 10.1109/ULTSYM.2017.8091551.

[30]. Saharkhiz N. et al. , "Harmonic motion imaging of human breast masses: an in vivo clinical feasibility," Sci. Rep, vol. 10, no. 1, pp. 1–13, Dec. 2020, doi: 10.1038/s41598-020-71960-5. [PubMed: 31913322]

[31]. Han Y, Wang S, Payen T, and Konofagou E, "Fast lesion mapping during HIFU treatment using harmonic motion imaging guided focused ultrasound (HMIgFUS) in vitro and i*n vivo*," Phys. Med. Biol, vol. 62, no. 8, pp. 3111–3123, Apr. 2017, doi: 10.1088/1361-6560/aa6024. [PubMed: 28323638]

[32]. Chen H. et al. , "Harmonic motion imaging for abdominal tumor detection and high-intensity focused ultrasound ablation monitoring: An in vivo feasibility study in a transgenic mouse model of pancreatic cancer," IEEE Trans. Ultrason. Ferroelectr. Freq. Control, vol. 62, no. 9, pp. 1662–1673, Sep. 2015, doi: 10.1109/TUFFC.2015.007113. [PubMed: 26415128]

[33]. Han Y, Wang S, Hibshoosh H, Taback B, and Konofagou E, "Tumor characterization and treatment monitoring of postsurgical human breast specimens using harmonic motion imaging (HMI)," Breast Cancer Res., vol. 18, no. 1, p. 46, Dec. 2016, doi: 10.1186/s13058-016-0707-3. [PubMed: 27160778]

[34]. Saharkhiz N. et al. , "Harmonic motion imaging of human breast masses: an in vivo clinical feasibility," Sci. Rep, p. In press, 2020, doi: 10.1038/s41598-020-71960-5.

[35]. Ebbini ES and Cain CA, "A Spherical-Section Ultrasound Phased Array Applicator for Deep Localized Hyperthermia," IEEE Trans. Biomed. Eng, vol. 38, no. 7, pp. 634–643, 1991, doi: 10.1109/10.83562. [PubMed: 1879855]

[36]. Damianou C. and Hynynen K, "Focal spacing and near-field heating during pulsed high temperature ultrasound therapy," Ultrasound Med. Biol, vol. 19, no. 9, pp. 777–787, Jan. 1993, doi: 10.1016/0301-5629(93)90094-5. [PubMed: 8134978]

[37]. Goss SA, "Sparse random ultrasound phased array for focal surgery," IEEE Trans. Ultrason. Ferroelectr. Freq. Control, vol. 43, no. 6, pp. 1111–1121, 1996, doi: 10.1109/58.542054.

[38]. Zanotel M. et al. , "Automated breast ultrasound: basic principles and emerging clinical applications," Radiol. Med, vol. 123, no. 1, pp. 1–12, Jan. 2018, doi: 10.1007/s11547-017-0805-z. [PubMed: 28849324]

[39]. Gavrilovi LR, "A theoretical assessment of the relative performance of spherical phased arrays for ultrasound surgery," IEEE Trans. Ultrason. Ferroelectr. Freq. Control, vol. 47, no. 1, pp. 125–139, Jan. 2000, doi: 10.1109/58.818755. [PubMed: 18238524]

[40]. Ebbini ES, Umemura SI, Ibbini M, and Cain CA, "A Cylindrical-Section Ultrasound Phased-Array Applicator for Hyperthermia Cancer Therapy," IEEE Trans. Ultrason. Ferroelectr. Freq. Control, vol. 35, no. 5, pp. 561–572, 1988, doi: 10.1109/58.8034. [PubMed: 18290188]

[41]. Chaplin V. and Caskey CF, "Multi-focal HIFU reduces cavitation in mild-hyperthermia," J. Ther. Ultrasound, vol. 5, no. 1, Apr. 2017, doi: 10.1186/s40349-017-0089-8.

[42]. X F. and K H, "Control of the necrosed tissue volume during noninvasive ultrasound surgery using a 16-element phased array," Med. Phys, vol. 22, no. 3, pp. 297–306, 1995, doi: 10.1118/1.597603. [PubMed: 7596319]

[43]. Wan H, "Ultrasound surgery: Comparison of strategies using phased array systems," IEEE Trans. Ultrason. Ferroelectr. Freq. Control, vol. 43, no. 6, pp. 1085–1098, 1996, doi: 10.1109/58.542052.

[44]. Hand JW, Shaw A, Sadhoo N, Rajagopal S, Dickinson RJ, and Gavrilov LR, "A random phased array device for delivery of high intensity focused ultrasound," Phys. Med. Biol, vol. 54, no. 19, pp. 5675–5693, Sep. 2009, doi: 10.1088/0031-9155/54/19/002. [PubMed: 19724099]

[45]. Y H, R A, ML S, and K H, "Opening the Blood-Brain Barrier with MR Imaging-guided Focused Ultrasound: Preclinical Testing on a Trans-Human Skull Porcine Model," Radiology, vol. 282, no. 1, pp. 123–130, Jan. 2017, doi: 10.1148/RADIOL.2016152154. [PubMed: 27420647]

[46]. Basavarajappa L, Rijal G, and Hoyt K, "Multifocused ultrasound therapy for controlled microvascular permeabilization and improved drug delivery," IEEE Trans. Ultrason. Ferroelectr. Freq. Control, pp. 1–1, Sep. 2020, doi: 10.1109/tuffc.2020.3026697.

[47]. Hertzberg Y, Naor O, Volovick A, and Shoham S, "Towards multifocal ultrasonic neural stimulation: pattern generation algorithms," J. Neural Eng, vol. 7, no. 5, p. 056002, Aug. 2010, doi: 10.1088/1741-2560/7/5/056002.

[48]. Han Y, Payen T, Wang S, and Konofagou E, "Focused Ultrasound Steering for Harmonic Motion Imaging," IEEE Trans. Ultrason. Ferroelectr. Freq. Control, vol. 65, no. 2, pp. 292–294, Feb. 2018, doi: 10.1109/TUFFC.2017.2781188. [PubMed: 29424694]

[49]. Jianwen Luo J. and Konofagou EE, "A fast normalized cross-correlation calculation method for motion estimation," IEEE Trans. Ultrason. Ferroelectr. Freq. Control, vol. 57, no. 6, pp. 1347–1357, Jun. 2010, doi: 10.1109/TUFFC.2010.1554. [PubMed: 20529710]

[50]. SA L, HAS K, and EE K, "Displacement Imaging During Focused Ultrasound Median Nerve Modulation: A Preliminary Study in Human Pain Sensation Mitigation," IEEE Trans. Ultrason. Ferroelectr. Freq. Control, vol. 68, no. 3, pp. 526–537, Mar. 2021, doi: 10.1109/TUFFC.2020.3014183. [PubMed: 32746236]

[51]. Palmeri ML, Mcaleavey SA, Trahey GE, and Nightingale KR, "Ultrasonic Tracking of Acoustic Radiation Force-Induced Displacements in Homogeneous Media." Accessed: Mar. 24, 2020. [Online]. Available: http://www.es.oersted.dtu.dk/staff/jaj/field/.

[52]. Chapelon JY et al. , "Feasibility of tissue ablation using high intensity electronically focused ultrasound," Proc. IEEE Ultrason. Symp, vol. 2, pp. 1211–1214, 1993, doi: 10.1109/ULTSYM.1993.339615.

[53]. Dupenloup F, Chapelon JY, Cathignol DJ, and Sapozhnikov OA, "Reduction of the grating lobes of annular arrays used in focused ultrasound surgery," IEEE Trans. Ultrason. Ferroelectr. Freq. Control, vol. 43, no. 6, pp. 991–998, 1996.

[54]. Gavrilov LR, Hand JW, Abel P, and Cain CA, "A method of reducing grating lobes associated with an ultrasound linear phased array intended for transrectal thermotherapy," IEEE Trans. Ultrason. Ferroelectr. Freq. Control, vol. 44, no. 5, pp. 1010–1017, 1997, doi: 10.1109/58.655626.

[55]. Lu M, Wan M, Xu F, Wang X, and Zhong H, "Focused beam control for ultrasound surgery with spherical-section phased array: Sound field calculation and genetic optimization algorithm," IEEE Trans. Ultrason. Ferroelectr. Freq. Control, vol. 52, no. 8, pp. 1270–1290, Aug. 2005, doi: 10.1109/TUFFC.2005.1509786. [PubMed: 16245597]

[56]. Vappou J, Hou GY, Marquet F, Shahmirzadi D, Grondin J, and Konofagou EE, "Non-contact, ultrasound-based indentation method for measuring elastic properties of biological tissues using harmonic motion imaging (HMI)," Phys Med Biol, vol. 60, no. 7, pp. 2853–2868, 2015, doi: 10.1088/0031-9155/60/7/2853. [PubMed: 25776065]
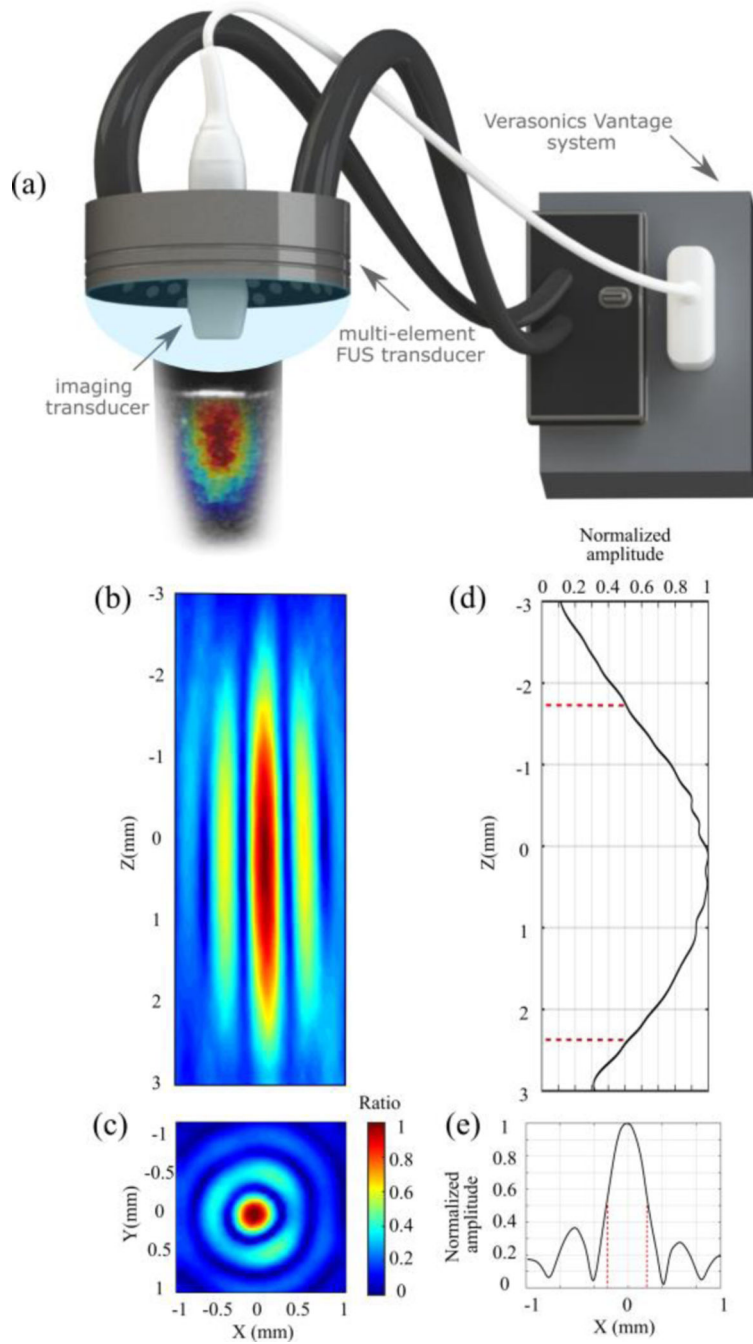
Fig. 1.
Single system HMI experimental setup and FUS transducer beam profile measured with a hydrophone. (a) The HMI assembly is comprised of a 4.5 MHz 128-element FUS transducer coaligned with a 7.8 MHz phased-array imaging transducer. The FUS transducer was driven with the first 128 channels of a 256 HIFU Verasonics system, while the imaging transducer was driven through the other 128 channels of the Vantage system. (b,c) Normalized hydrophone measured pressure profile of the FUS transducer in axial plane and (d,e) transverse plane. The full width half maximum (FWHM) is denoted by red dashed lines.
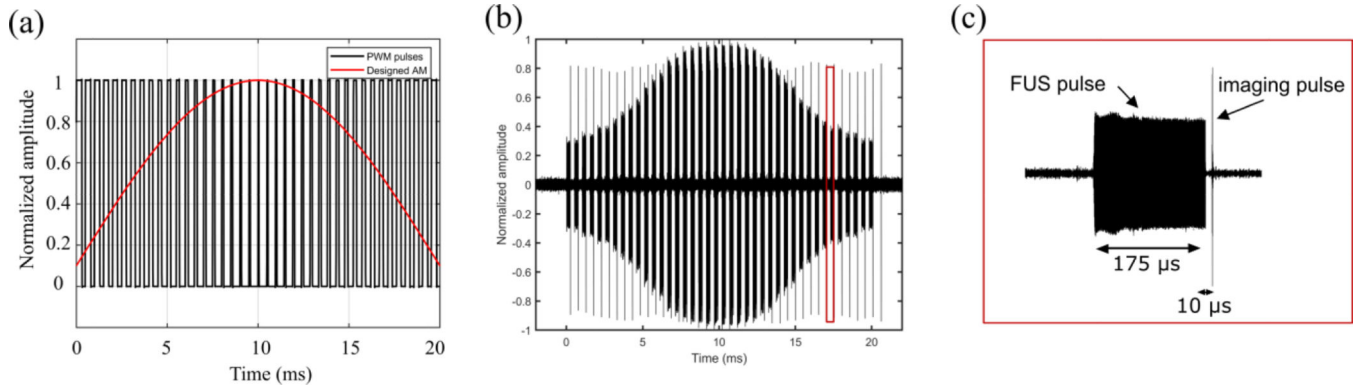
Fig. 2.
HMI pulse sequence. (a) Each cycle of the AM pulse (period: 20 ms) was divided into 40 segments. The relative width of each segment was proportional to $\frac{2}{\pi} sin^{-1}\left(\frac{9\cos(x) + 11}{20}\right)$ at each segment,. (b) Hydrophone measured output of the FUS transducer showing one cycle of the 50-Hz modulation. Therefore, 40 different transmit waveforms were synthesized each with a period of 500 μs and relative pulse width as showed. (c) Magnification of the region delineated with red dashed lines Each segment is composed of a 175μs pulse at the frequency of 4.5 MHz (35% duty cycle), interleaved (10 μs separation) by a 1.5 cycles imaging pulse. This pulse sequence resulted in an imaging frame rate of 2000 kHz.
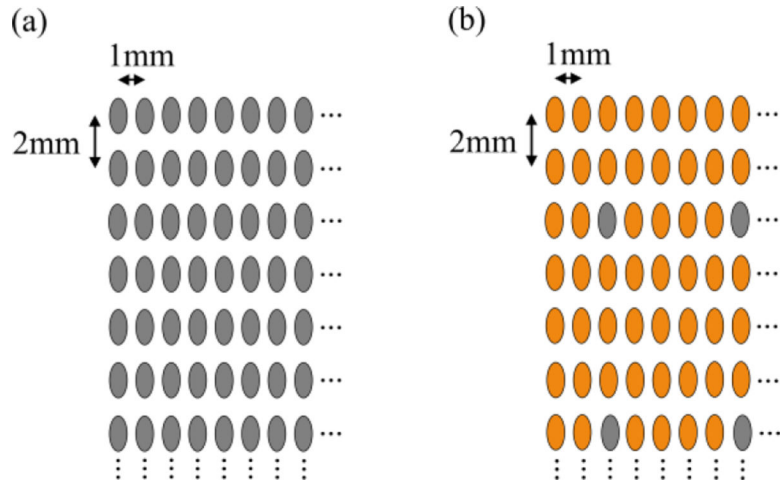
Fig. 3.
Schematic of the two scenarios for imaging inclusions embedded within the tissue mimicking phantom. (a) The transducer assembly was moved mechanically in a 2-D point-by-point raster scan regimen using the 3-D positioner where the points were separated 2 mm axially and 1 mm laterally. The acoustic force was only generated at the geometric focus (gray ellipses). (b) The transducer assembly was moved mechanically using the 3-D positioner where the points were separated 8 mm axially and 4 mm laterally. The acoustic force was generated at the geometric focus (gray ellipses). At each of these points, the focus was electronically moved in both directions (orange ellipses) with the step sizes of 2 mm axially and 1 mm laterally.
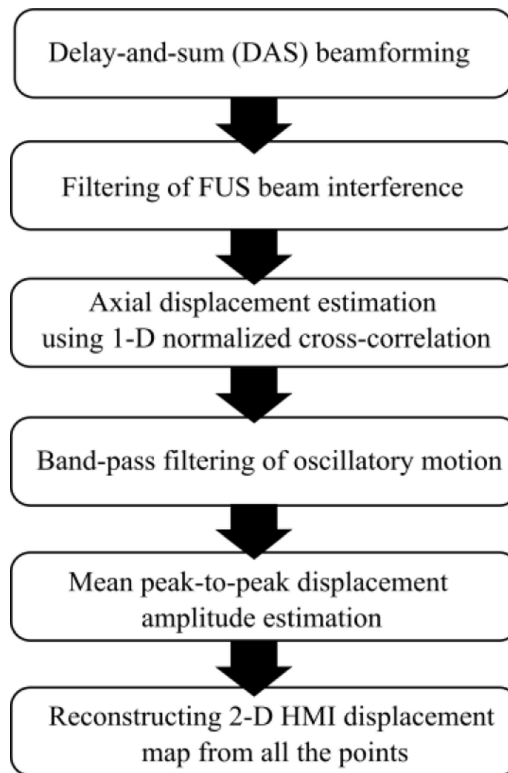
Fig. 4.
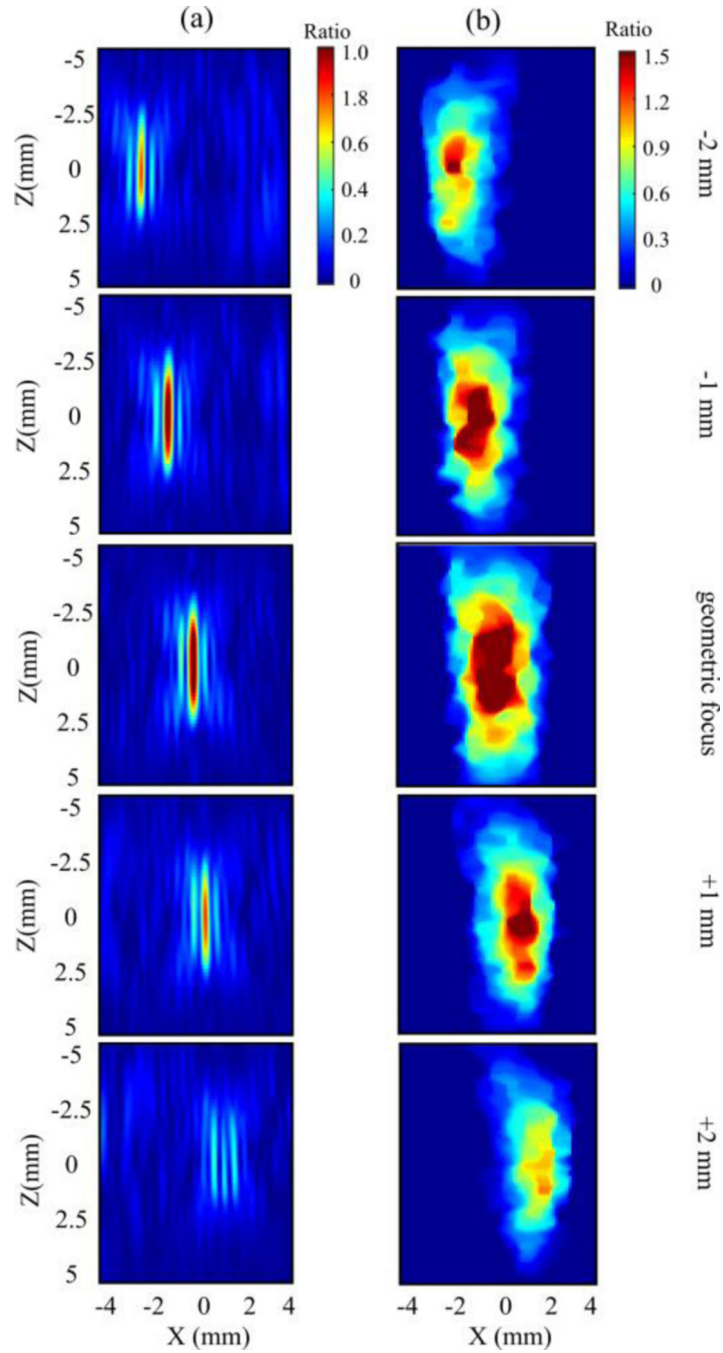Data processing pipeline to generate 2-D HMI displacement maps
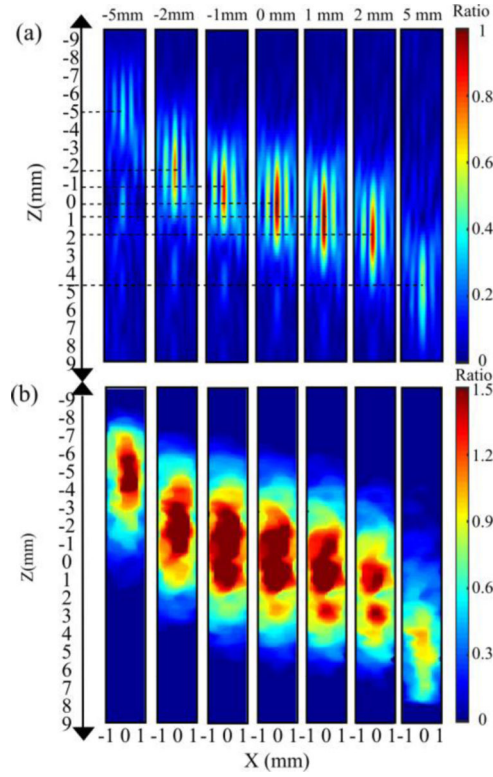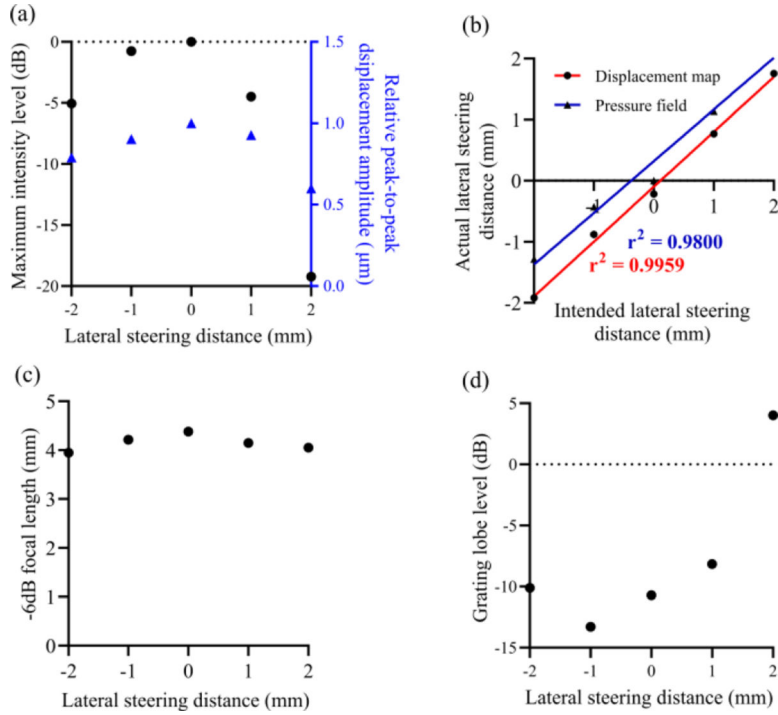
Fig. 5.

(a) Normalized acoustic pressure profiles with respect to the maximum acoustic pressure at the geometric focus, measured with the bullet hydrophone for axial electronic steering distances of −5, −2, −1, 0, 1, 2 and 5 mm from the geometric focus. (b) Corresponding normalized 2-D HMI displacement maps with respect to the maximum displacement amplitude at the geometric focus measured within the background of the tissue-mimicking phantom. The frames are shown at 10 ms after triggering a 20-ms HMI signal (AM frequency: 50 Hz).
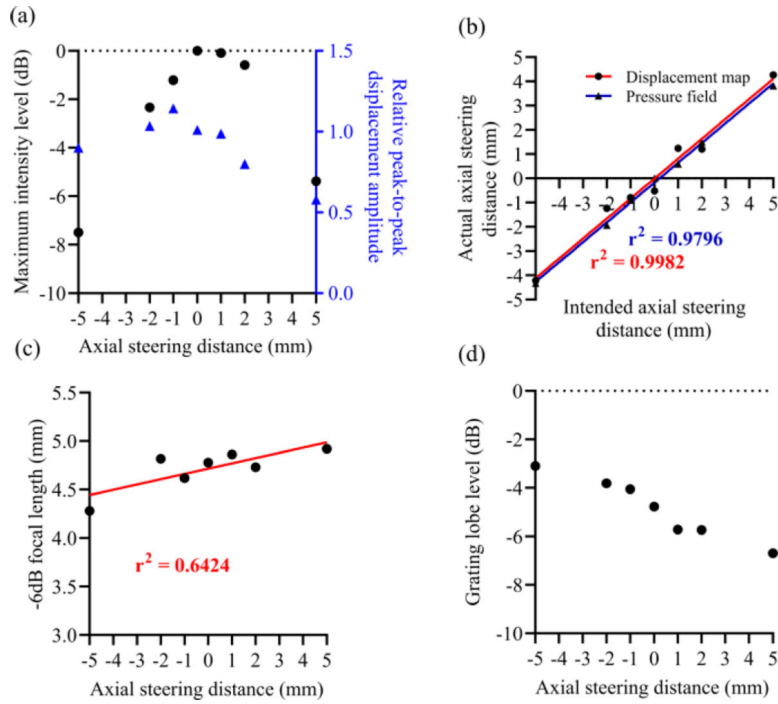
Fig. 6.
(a) Relative acoustic pressure (black) as a function of axial steering distance with respect to the pressure at the geometric focus measured with the bullet hydrophone in free field and relative maximum peak-to-peak displacement amplitude (blue) with respect to the maximum displacement at the geometric focus as a function of axial steering distance from displacement maps shown in Fig. 4b. (b) The location of the point with maximum acoustic pressure measured with the hydrophone (triangle) and location of the point with maximum peak-to-peak HMI displacement amplitude (circle) versus the intended axial steering distance.(c) Axial length of the focus as a function of the axial steering distance measured with the hydrophone in free field. (d) The maximum intensity of the grating lobes as a function of axial steering distance.

Fig. 7.
(a) Normalized acoustic pressure profiles with respect to the maximum acoustic pressure at the geometric focus, measured with the bullet hydrophone for lateral steering distances of −2, −1, 0, 1and 2 mm from the geometric focus, (b) Corresponding normalized 2-D HMI displacement maps with respect to the maximum displacement amplitude at the geometric focus, measured within the background of the tissue-mimicking phantom. The frames are shown at 10 ms after triggering a 20 ms HMI signal (AM frequency: 50 Hz).

Fig. 8.
(a) Normalized maximum intensity level (black) as a function of lateral steering distance with respect to the intensity at the geometric focus measured with the bullet hydrophone in free field and relative maximum peak-to-peak displacement amplitude (blue) with respect to the maximum displacement at the geometric focus as a function of lateral steering distance from displacement maps shown in Fig. 7b. (b) The location of the point with maximum acoustic pressure measured with the hydrophone (triangle) and location of the point with maximum peak-to-peak HMI displacement amplitude (circle) versus the intended axial steering distance.(c) Axial length of the focus as a function of the axial steering distance measured with the hydrophone in free field. (d) The relative maximum pressure of the grating lobes with respect to the one at the geometric focus as a function of axial steering distance.
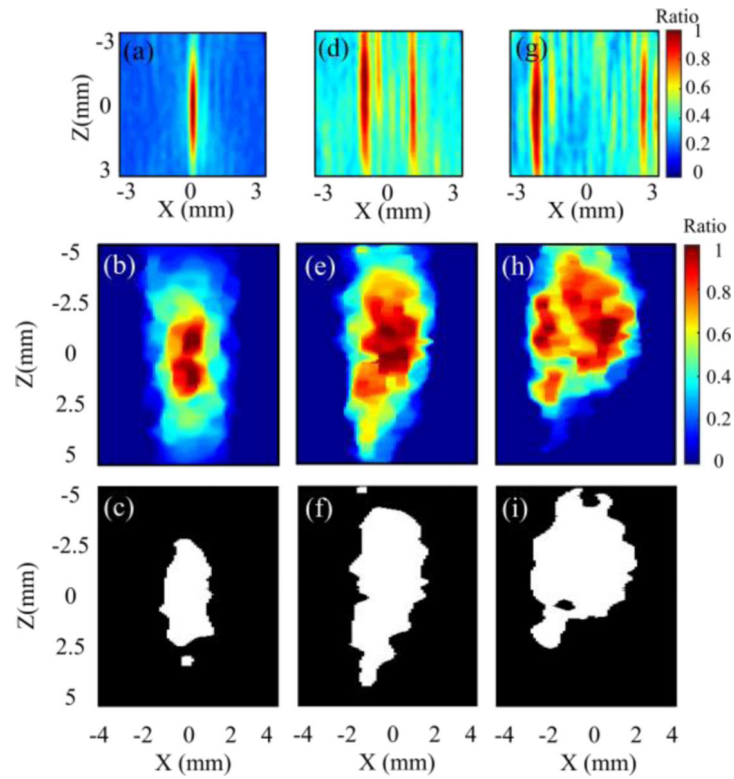
Fig. 9.
Normalized acoustic pressure maps with respect to the maximum pressure at each map (first row), normalized 2-D HMI displacement maps with respect to the maximum displacement at each map (second row) and corresponding −6 dB displacement regions (third row) for (a, b, c) a single focus, (d, e, f) 2 foci separated by 2 mm in the lateral direction and (g,h,i) 2 foci separated by 4 mm in the lateral direction.
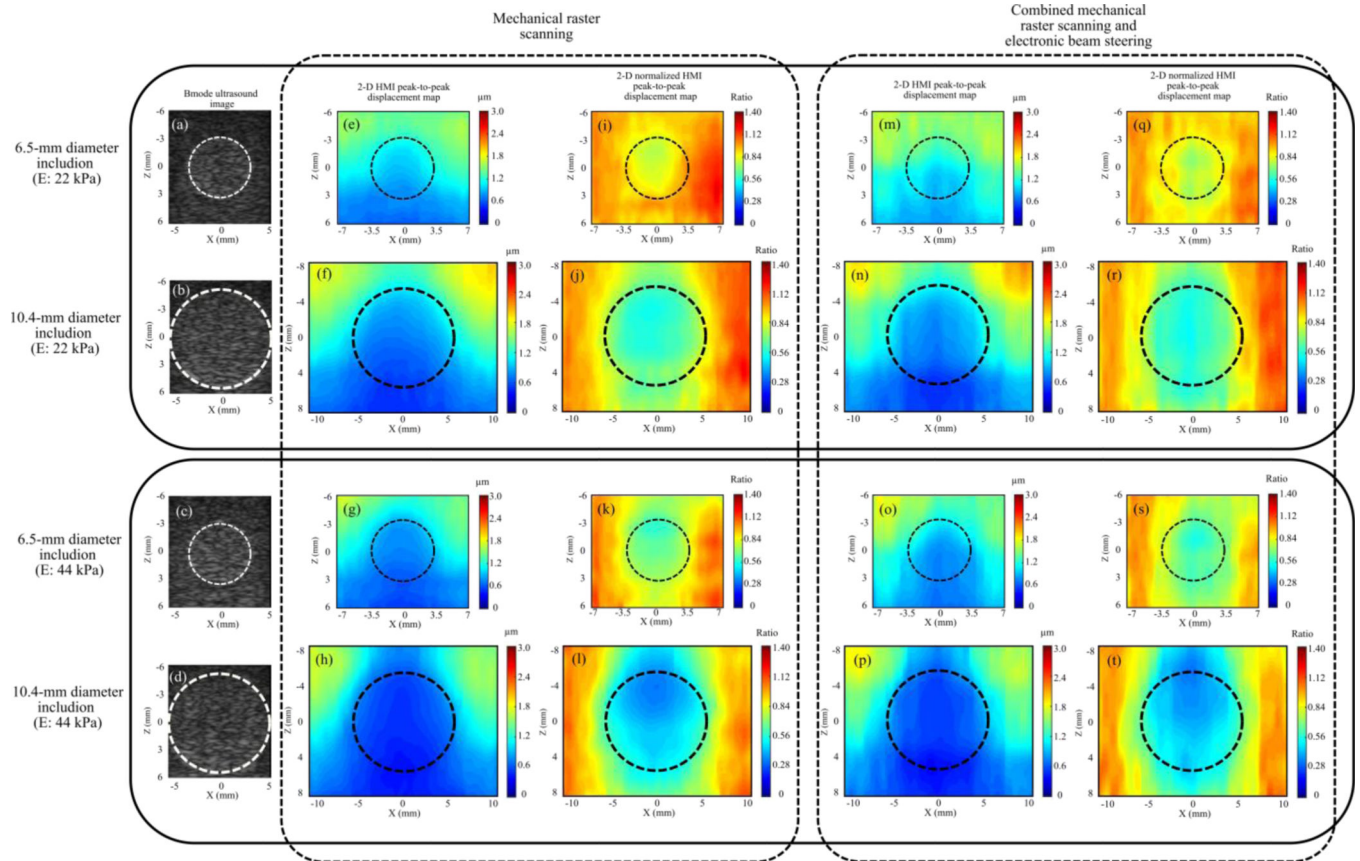
Fig. 10.
(a-d) B-mode ultrasound images, (e-h) 2-D HMI displacement maps and (i-l) 2-D normalized displacement maps of inclusions where data was acquired through mechanical raster scanning, (m-p) 2-D HMI displacement maps and (q-t) 2-D normalized displacement maps of inclusions where data was acquired through combined mechanical raster scanning and electronic beam steering. The inclusions are delineated using black dashed lines.
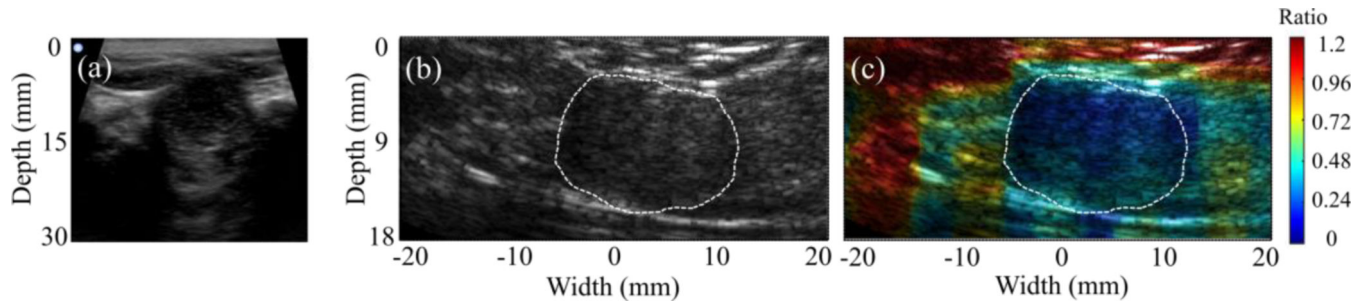
Fig. 11.
(a) B-mode image acquired with clinical ultrasound scanner, (b) B-mode image acquired with the 7.8 –MHz imaging transducer and (c) normalized HMI displacement map overlaid on the B-mode image of an *in vivo* human breast tumor. The tumor was characterized as a 2.8cm Fibroadenoma. The tumor is delineated with white dashed lines.

TABLE I

RASTER SCAN PARAMETERS

	6.5-mm diameter inclusion	10.4-mm diameter inclusion
Mechanical raster scanning		
Number of points in the lateral direction	15	21
Number of points in the axial direction	7	9
Lateral step size (mm)	1	1
Axial step size (mm)	2	2
Electronic beam steering + mechanical raster scanning		
Number of points in the lateral direction	4	6
Number of points in the axial direction	2	3
Lateral step size (mm)	4	4
Axial step size (mm)	8	8